



Axial load tests and numerical modeling of single-helix piles in cohesive and cohesionless soils

Weidong Li¹ · Lijun Deng¹

Received: 22 April 2017 / Accepted: 17 April 2018 / Published online: 30 April 2018
© Springer-Verlag GmbH Germany, part of Springer Nature 2018

Abstract

Small-diameter helical piles have been increasingly used in Western Canada, but there is a lack of research. The present research investigates the axial behavior of three types of small-diameter single-helix piles. Twenty-six helical piles were installed and loaded axially in a cohesive and a cohesionless soil sites. The limit state capacities are attained or extrapolated from the load versus displacement curves following Chin's hyperbolic assumption. It is found that the hyperbolic assumption can closely predict the load versus displacement curves of the helical piles. The torque factor K_t was smaller for the larger pile shaft diameter in the homogeneous site, whereas in the heterogeneous site K_t is substantially affected by soil heterogeneity around the helix. To further understand the axial behavior of the tested piles, a beam-on-nonlinear-Winkler-foundation model is developed on the platform of the Open System for Earthquake Engineering Simulation, which is a finite element software framework for the computation of soil and structural systems. A parametric analysis is carried out to determine the best estimate of ineffective length, the equivalent shaft length where the shaft resistance is zero. It is shown that the numerical model with ineffective length of four helix diameters can properly simulate the axial load versus displacement behavior.

Keywords Axial behavior · BNWF model · Field load test · Ineffective length · Single-helix pile

1 Introduction

A helical pile is a deep foundation system consisting of a circular or square shaft and one or more helices affixed to the shaft. The helical pile configuration increases the axial base resistance, facilitates the installation, and enables the reusability. These advantages have increased the applications of helical piles in the past decades to support pipelines, transmission towers, commercial buildings, and offshore structures.

The axial behavior of helical piles is characterized by the limit capacity Q_L , the critical displacement Z_c where the axial resistance reaches Q_L , and the load versus displacement curve. A number of axial field load tests of single-helix piles with shaft diameter d greater than 150 mm have been conducted (e.g., [1, 14, 16, 25, 26, 32]);

these tests determined the ratio of ultimate capacity to installation torque, K_t , and some of these studies analyzed the axial load versus displacement relationship. The first objective of the present study is to further elaborate the axial load transfer mechanism of small-diameter piles via field load tests. The present study selected three types of single-helix piles with shaft diameters of 73, 89, and 114 mm, respectively. The field load tests included 15 compressive tests and 11 tensile tests at two test sites dominated by cohesive and cohesionless soils, respectively. The ultimate capacities Q_{ult} were observed; the limit capacities Q_L were observed or extrapolated following Chin's hyperbolic assumption [11]. The axial ultimate capacity design of helical piles in the industry is typically based on the empirical torque factor K_t . It has been found that K_t primarily varies with the soil type, pile dimension, and soil strength profile [27, 30]. The K_t values of the test piles in the present program are determined from the field test results and compared to that in the literature. The effects of soil heterogeneity on K_t are elaborated according

✉ Lijun Deng
ldeng@ualberta.ca

¹ Department of Civil and Environmental Engineering,
University of Alberta, Edmonton, Canada

to the profile of the in situ soil properties obtained from cone penetration tests (CPTs).

The test piles in the present study were not instrumented; therefore, it is difficult to interpret the axial soil–pile interaction in the tests. A beam-on-nonlinear-Winkler-foundation (BNWF) numerical model is developed for the soil–helical pile simulations taking advantage of the existing soil–pile interaction in the literature. The BNWF method simplifies the soil–structure interaction (SSI) into a series of soil reaction springs. The BNWF method has been used extensively in SSI research but not yet for helical piles. The present study thus serves as a verification of the BNWF method in helical pile applications. Input parameters of the BNWF model are determined from soil parameters obtained from the CPT results. This numerical modeling is accomplished on the platform of Open System for Earthquake Engineering Simulation [22], a finite element framework for the computation of soil and structural system.

The shaft resistance of helical piles was found to be zero within a significant extent above the top helix [31] in compression and within a varied length near the ground surface in tension [23, 31]. Rao et al. [23] defined the equivalent shaft length where the shaft resistance is zero as the *ineffective length* l_{ineff} ; based on laboratory tests, the estimated l_{ineff} was $1.4D$ – $2.3D$ in the very soft clay [23], but the test results of Zhang [32] for l_{ineff} in stiff clays and medium to dense sands are different than the results of Rao et al. [23] for soft clay. Therefore, the BNWF model is used to conduct a parametric analysis of l_{ineff} to give an estimate of l_{ineff} for the present pile types and soil states.

2 Field load tests

The field test program consisted of 15 axial compressive and 11 axial tension tests of helical piles at two test sites. Three types of small-diameter single-helix piles with differing dimensions were chosen for the test program. Field load tests conform to the procedures in ASTM standard D1143 [4] for axial compression tests and D3689 [5] for axial tension tests.

2.1 Subsurface investigation

The research program selected two test sites. As shown in Fig. 1, Site 1 on the University Farm is located in Edmonton, Alberta, Canada. Site 2 at a sand pit is located 7.5 km north of the town of Bruderheim, Alberta, Canada. The sites were used traditionally as field stations of pile load tests because they represent typical soils of Alberta. The soil at Site 1 is the glaciolacustrine clay deposited by Glacial Lake Edmonton that covered Edmonton and

neighboring areas from approximately 12,000–10,000 years ago; the soil at Site 2 was formed as the beach sand dunes at the shoreline of Glacial Lake Edmonton [15].

Three CPTs were performed at Site 1 and four CPTs at Site 2 to a minimum depth of 7.0 m below ground surface (BGS), which is sufficiently greater than the embedment of the longest piles tested in the present program. The CPT results shown in Figs. 2 and 3 include the cone tip resistance q_c , sleeve friction f_s , and pore pressure u_2 . The soil behavior type (SBT) was evaluated following the guideline of Robertson and Cabal [24]. As shown in Fig. 2, the soil at Site 1 is: top soil (0–1 m) underlain by fairly homogeneous clay (down to 5 m BGS). As shown in Fig. 3, the soil at Site 2 is mainly sand to sandy silt to 4 m BGS underlain by the interbedded layers of sandy silt, clayey silt, and silty clay from 4 m to 5.8 m BGS.

The profile of undrained shear strength s_u is estimated using Eq. (1) [24]:

$$s_u = \frac{q_t - \sigma_v}{N_{kt}} \quad (1)$$

where N_{kt} is the cone factor, q_t is the cone resistance corrected according to the pore pressure, and σ_v is the vertical total stress. N_{kt} of 15 is selected, which is the median as per Robertson and Cabal [24]. Unconfined compressive strength (UCS) tests and laboratory vane shear tests were conducted on intact Shelby tube samples at Site 1 collected in early 2016. The measured s_u is shown in Fig. 2 to justify the selection of N_{kt} . It is observed that the measured s_u agrees with the s_u interpreted from the CPT results. The groundwater table (GWT) at Site 1 at 4.8 m BGS was measured directly by detecting the water level in the boreholes left by the reaction piles, 4 weeks after the reaction piles were removed.

The internal friction angle ϕ' of soils at Site 2 is estimated using Eq. (2) [24]:

$$\tan \phi' = \frac{1}{2.68} \left[\log \left(\frac{q_c}{\sigma'_v} \right) + 0.29 \right] \quad (2)$$

where ϕ'_v is the vertical effective stress. A polyline is shown in Fig. 3 to represent the average values of ϕ' . The GWT at Site 2 was about 3.0 m BGS, measured inside the reaction piles at the end of the load tests at Site 2.

2.2 Configuration and installation of test piles

The configuration of a typical single-helix pile is shown in Fig. 4. The shaft diameter d of the three types of piles ranges from 73 to 114 mm, the helix diameter D from 305 to 406 mm, and the pile length L from 2.44 to 4.57 m. The test piles have a D/d ratio ranging from 3.6 to 4.2, which is a common configuration for small-diameter helical piles

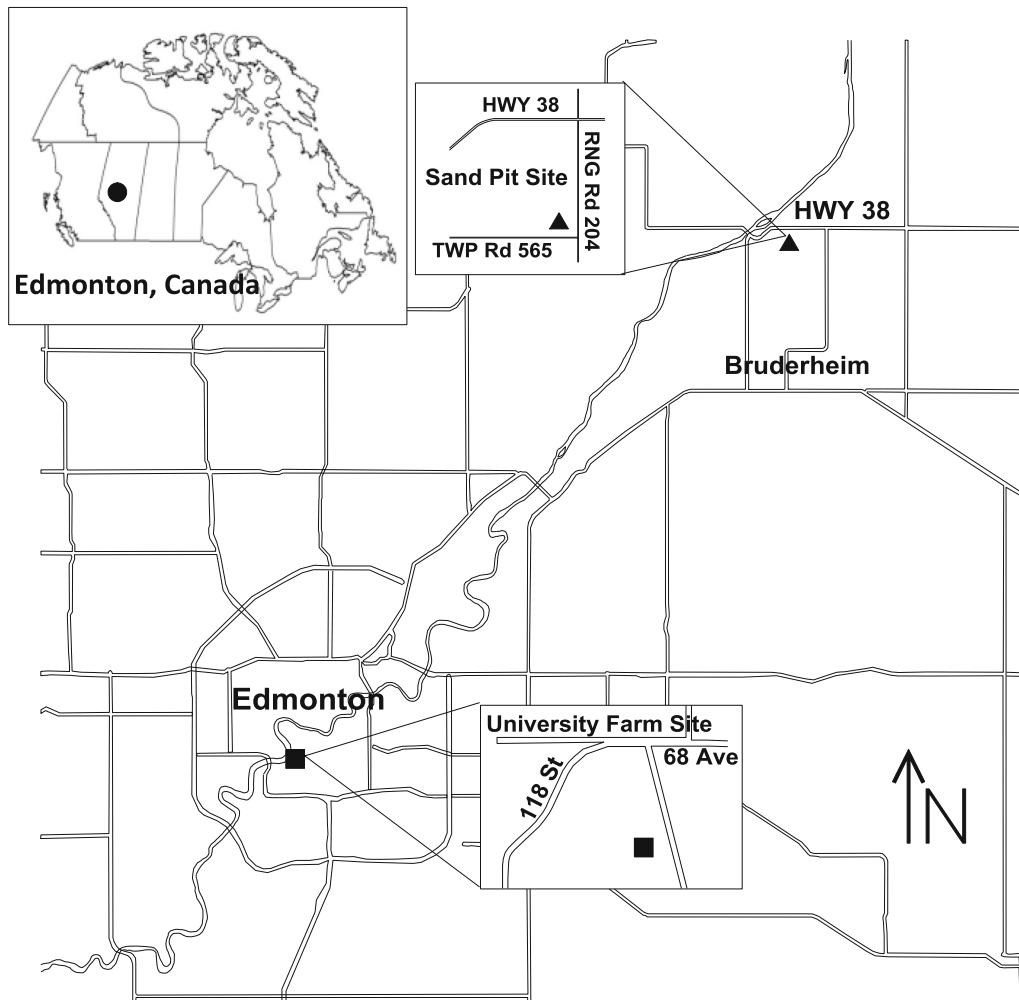


Fig. 1 Locations of test sites: Site 1 at the University Farm and Site 2 at a sand pit

used in Western Canada. For all the test piles, the wall thickness of the pipe is 7.8 mm, and the thickness of the helices is 9.5 mm. Table 1 summarizes the test pile configurations. About 300 mm of pile shaft was left above the ground surface to allow for the setup of apparatus. A pile cap was welded to the head of every pile to seat the hydraulic jack.

Figure 5 shows the layout of the test piles, reaction piles, and the CPT boreholes at Site 1. The center-to-center spacing between every two adjacent piles was 2.87 m, which is greater than $5D$ ($0.508 \text{ m} \times 5$) of the larger pile (i.e., the reaction pile) to minimize the pile–pile interaction, following the recommendation of ASTM [4, 5]. The helical piles were screwed into the ground using a torque head mounted to an excavator. To minimize the soil disturbance during installation, the leading edge of the helix is sharpened, the helical blade is fabricated to form a right angle to the shaft, and the axial advancing rate was controlled at one pitch length per revolution.

2.3 Load test reaction system

The reaction system for the compression load tests consists of two large reaction piles and a reaction I-beam connected to the top of the reaction piles via threaded rods as shown in Figs. 6 and 7a. During the compressive loading, the load was transferred from the hydraulic jack via the reaction beam to the reaction piles. The reaction system for tension load tests includes additional four threaded rods and a steel plate on the top of the load cell as shown in Fig. 7b. During the tensile loading, the pullout load was transferred from the hydraulic jack via the steel plate and four rods to the test pile. The reaction helical pile is significantly larger than the test piles to provide much greater axial capacity; the length of the reaction piles is 6.9 m, the shaft diameter is 0.36 m, and the helix diameter is 0.76 m (two helices); the measured displacements of the reaction piles in all tests were trivial. Pipe rotation occurred in the first load test due to the lack of resisting moment about the pile axis. This rotation will not happen in the practice because of the

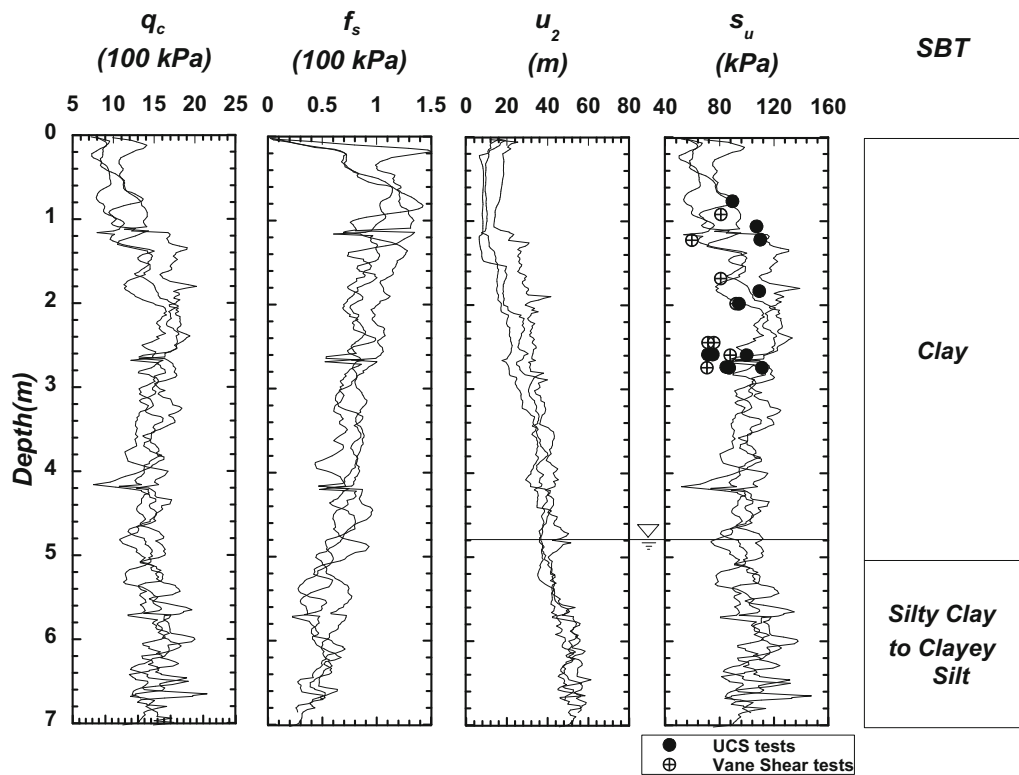


Fig. 2 CPT profile of Site 1

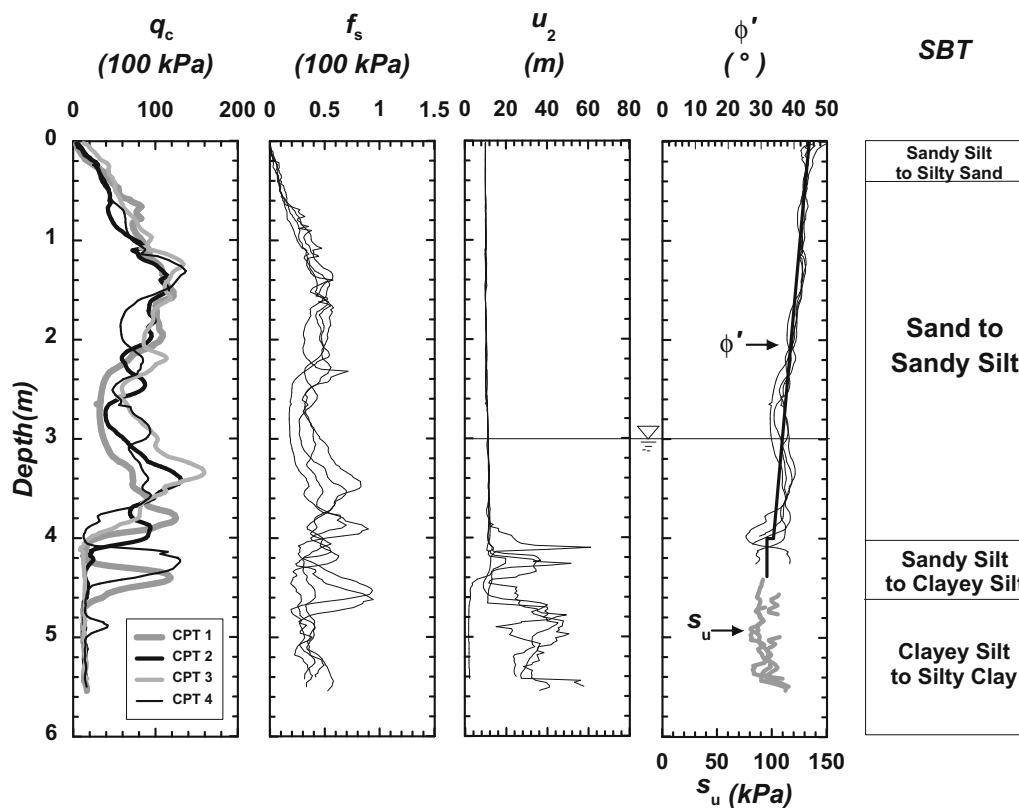


Fig. 3 CPT profile of Site 2

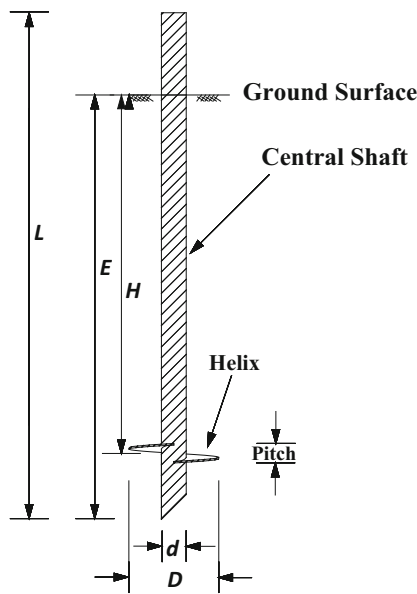


Fig. 4 Sketch of a typical single-helix pile

Table 1 Configurations of three types of test piles

Pile	Total length L (m)	Shaft diameter d (mm)	Helix diameter D (mm)	D/d	Helix embedment H (m)	Pitch P (mm)
P1	2.44	73	305	4.2	1.83	76
P2	3.05	89	356	4.0	2.44	76
P3	4.57	114	406	3.6	3.96	76

constraints exerted by the super structure, but in the present tests, the rotation can take place, change the pile axial performance, and disturb the data logger. Therefore, two hooks were welded to the pile cap and connected tightly to the reaction piles via two strong chains (Fig. 7b); the hooks effectively prevented the rotation in the following tests.

2.4 Load test measurement

The axial displacement was measured using two linear potentiometers (LP) and two dial gauges. The probes of LPs and dial gauges were placed on the leveled reference beams, and the bodies of the LP's and dial gauges were attached to the pile cap via magnetic bases. The average readings of the LPs are used as the pile displacements, and the dial gauges are for backup. The installation torque was measured at every 300 mm axial penetration during installation.

2.5 Testing procedure

The load tests were conducted conforming to ASTM D1143 (ASTM [4]) for compression and ASTM D3689 [5] for tension. For all of the axial load tests, each pile was loaded to the ultimate or limit failure state at an increment of 5% of the predicted capacity. We estimated the limit capacities of the helical piles according to the torque-factor method [17] using the final installation torques and estimated torque factor from the literature: 33 m^{-1} for P1, 25 m^{-1} for P2, and 20 m^{-1} for P3. After each load increment, a constant time interval of 5 min was applied to allow for stabilization of pile displacement. In the unloading phase, a decrement of 25% of the maximum load and a constant time interval of 10 min were applied. The load at the ultimate or limit state was maintained for 15 min trying to obtain a complete plastic stage of the load–displacement curve before the unloading. To allow for the soil setup (i.e., process of soil strength recovery) at the cohesive soil site, we waited for 3 weeks after installing the helical piles although 1-week waiting period is sufficient for soil setup at a clayey site.

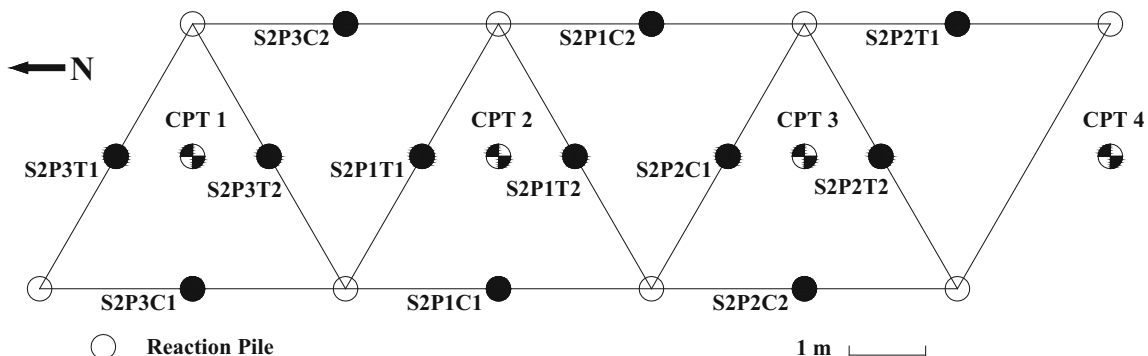


Fig. 5 Layout of test piles, reaction piles, and CPT boreholes at Site 2. Layout at Site 1 was similar

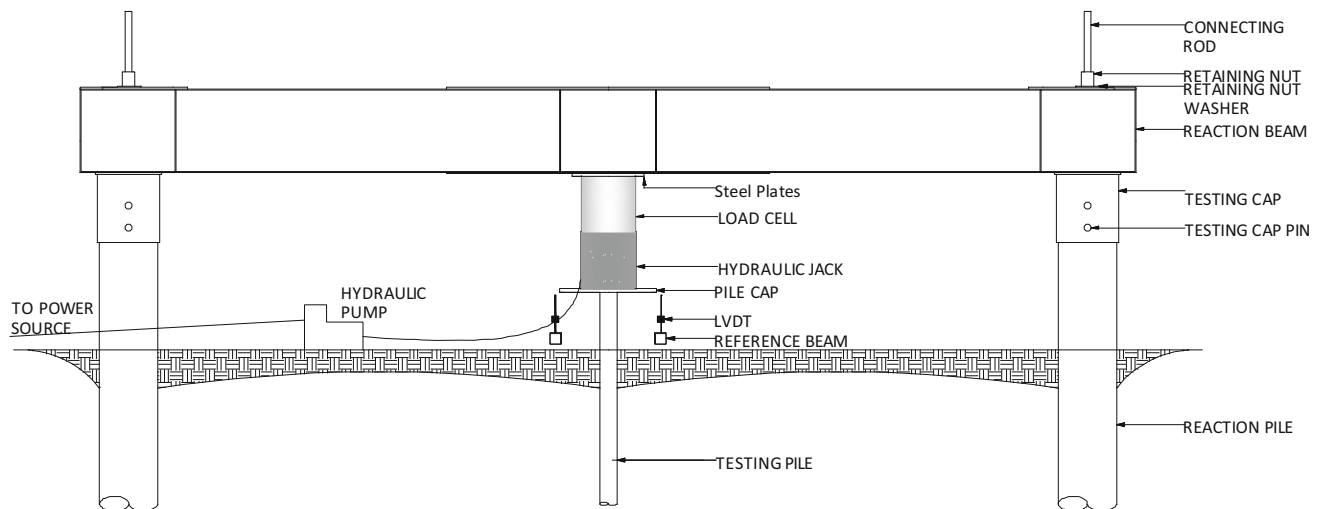


Fig. 6 Setup of axial compression tests

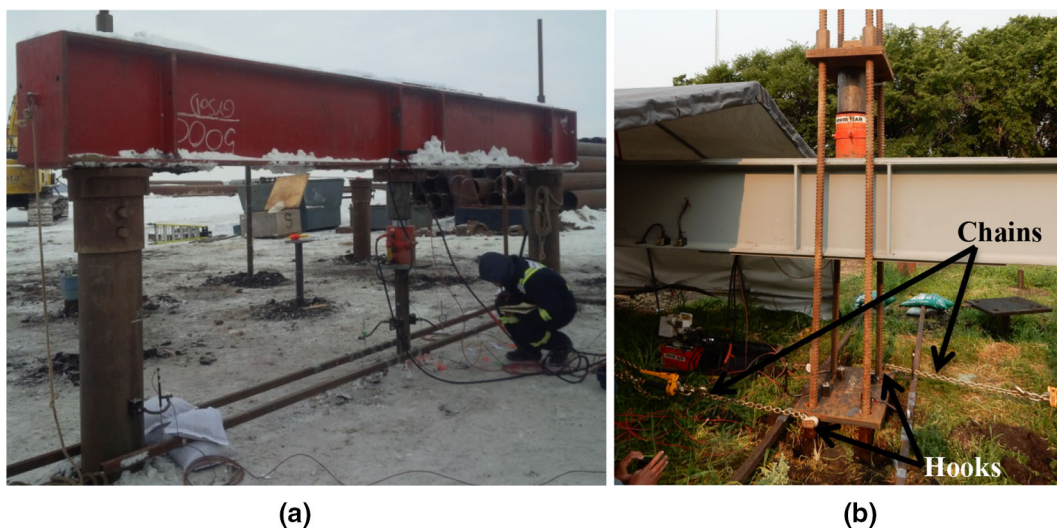


Fig. 7 Field test equipment and the setup: **a** compression; **b** tension

3 Field test results

Twenty-six axial compression and tension tests were carried out at two test sites. An ID that compiles the test site, pile type, load type, and the test sequence number was assigned to each test as presented in Table 2. Every test was repeated for at least two times to confirm the consistency of the test results. The test results showed that the discrepancy, with respect to the average capacity of every repetitive test group, was smaller than 5%.

3.1 Axial load versus displacement

Considering the repeated tests produced very similar $Q-w$ curves, only twelve curves of axial load (Q) versus displacement (w) are presented in Fig. 8 to represent all

soil types, load types, and pile types. Table 2 summarizes the measured ultimate capacity Q_{ult} at the axial displacement of 10% D . All the $Q-w$ curves consist of an initial linear segment, a transitioning segment, a plateau, and an unloading segment with a slope similar to the initial segment.

Figure 8a shows that for the curves of Site 1 (stiff clay, CGS [9]) the limit state was reached since the excessive displacement or plunging failure was observed. For every test at Site 1, Q_{ult} is equal to Q_L which is the axial load at the plunging failure stage; in addition, the compression capacity is generally greater than the tension capacity. Figure 8b shows that at Site 2 (medium to dense sand) the limit state was not reached because the plunging failure had not been observed despite the large axial displacement, except for test S2P3C1. For the load tests at Site 2, the limit

Table 2 Field test chronology and summary of results

Site	Pile	Load type	Test ID	Q_{ult}^1 (kN)	Q_L^2 (kN)	Q_L/Q_{ult} (%)	k_i^3 (N/mm)	R^2
1	P1	C	S1P1C1	52	52	100	18.9	0.998
			S1P1C2	48	48	100	21.0	0.999
			S1P1C3	56	56	100	17.9	0.998
		T	S1P1T1	48	48	100	20.9	1.000
			S1P1T2	44	44	100	22.5	0.999
	P2	C	S1P2C1	75	75	100	13.3	0.999
			S1P2C2	70	70	100	14.3	0.999
			S1P2C3	72	72	100	13.9	0.999
			S1P2C4	73	73	100	13.7	0.998
		T	S1P2T1	84	84	100	11.9	1.000
			S1P2T2	76	76	100	13.2	0.999
	P3	C	S1P3C1	112	112	100	8.9	1.000
S1P3C2			110	110	100	9.1	0.996	
S1P3T1			100	100	100	9.9	1.000	
2	P1	C	S2P1C1	104	114	110	8.8	0.985
			S2P1C2	96	108	113	9.3	0.987
			S2P1T1	79	88	111	11.4	0.999
		T	S2P1T2	73	88	121	11.4	0.994
			S2P2C1	126	143	113	7.0	0.993
	P2	C	S2P2C2	134	141	105	7.1	0.983
			S2P2T1	108	143	132	7.0	0.950
			S2P2T2	93	108	116	9.3	0.960
	P3	C	S2P3C1	128	135	105	7.4	0.996
			S2P3C2	114	112	98	8.9	0.997
			S2P3T1	178	189	106	5.3	0.991
		T	S2P3T2	164	180	110	5.6	0.984

Q_{ult} = load at the axial displacement equal to 10% of the helix diameter [28]

Q_L at Site 2 is extrapolated following Chin's hyperbolic criterion [11]

k_i = initial slope of the Q - w curve

R^2 = coefficient of determination of the fit lines of w/Q versus w curves

capacity (Q_L) of many piles might be too large to attain; in such case, Q_L was greater than the ultimate capacity (Q_{ult}) reached at the displacement of 10% D [28]. Malik et al. [20] compared the axial load–displacement behavior of helical piles to straight piles in sand and found that Q_L of helical piles were captured at 15% D which was greater than 10% D_{SP} (pile end diameter) for the straight piles. This difference may affect the numerical BNWF modeling of helical piles in further research because the existing soil reaction springs are based on load tests of straight piles. The compression capacity was generally greater than the tension capacity, except for S2P3C1. The reason for this exceptional behavior of S2P3C1 was the existence of the relatively weak cohesive soil pocket from 4.0 m to 6.0 m

BGS (shown in Fig. 3, CPT 1), which was under the helix of the pile P3 embedded at 4 m BGS; therefore, the failure zone created beneath the helix extended into the underlying clay and thus caused the reduction in the axial compression capacity.

Since Q_L was not observed in the tests at Site 2, it is necessary to extrapolate the test curves to attain Q_L . Chin [11] suggested that the Q - w curves of straight-shaft piles may follow the hyperbolic curve pattern according to:

$$Q = \frac{w}{c_1 w + c_2} \quad (3)$$

where c_1 is the inverse of Q_L (which is equal to Q when w approaches the infinity) and c_2 is the inverse of initial slope of the Q - w curve when w approaches zero. Equation (3) can be converted into:

$$\frac{w}{Q} = c_1 w + c_2. \quad (4)$$

By plotting w/Q versus w curves in the loading phase, one can determine c_1 and c_2 and then calculate the limit capacity and initial slope via:

$$Q_L = \frac{1}{c_1}, k_i = \frac{1}{c_2} \quad (5)$$

where k_i is the initial slope of the Q - w curve. We used Chin's method to assess whether the Q - w curves of helical piles follow the hyperbolic assumption and extrapolate the test curves to obtain Q_L for test piles at two sites. The w/Q versus w curves of the loading segment shown in Fig. 8 are plotted in Fig. 9 according to Eq. (4). The linearly regressed curves and several w/Q versus w equations are also shown in Fig. 9. It is shown in Fig. 9a that the hyperbolic assumption can perfectly interpret the Q versus w correlation of helical piles in cohesive soils at Site 1 because the w/Q versus w curves are nearly linear for most cases; for Site 2 as shown in Fig. 9b, the hyperbolic assumption works well, although not perfectly, for most of the Q versus w curves. In general, it is shown that Chin's hyperbolic assumption proposed for straight-shaft piles is capable of estimating the axial limit capacity of helical piles installed in the present two types of soils.

The Q_L values were obtained for all test piles according to Eq. (5) and are summarized in Table 2. At Site 1, Q_{ult} and Q_L are the same for all test piles. At Site 2, the Q_L of all test piles is generally greater than the measured Q_{ult} . Q_L of the test S2P3C2 is 98% of Q_{ult} because the Q - w curve exhibited the post-peak softening behavior. The initial stiffness k_i according to Eq. (5) is obtained for all test piles and summarized in Table 2. It shows that k_i is greater for piles at Site 1 than at Site 2, which confirms that the rate of resistance mobilization in cohesive soils is greater than in cohesionless soils at early stage of displacement. The

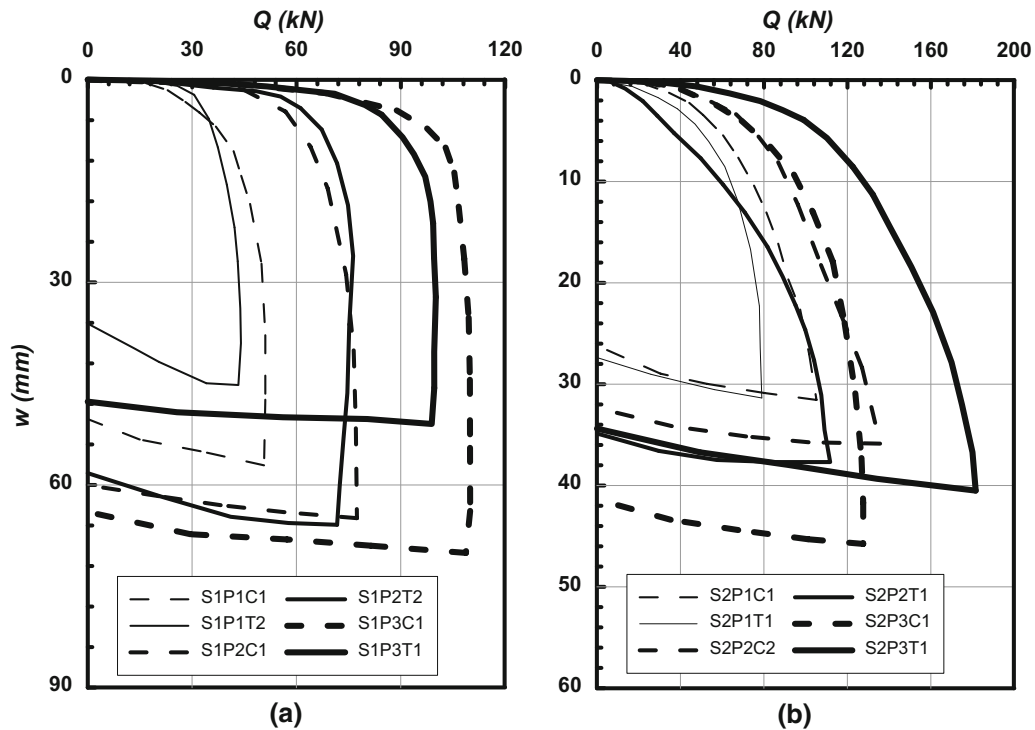


Fig. 8 Selected axial load Q versus displacement w curves of piles at: a Site 1 and b Site 2

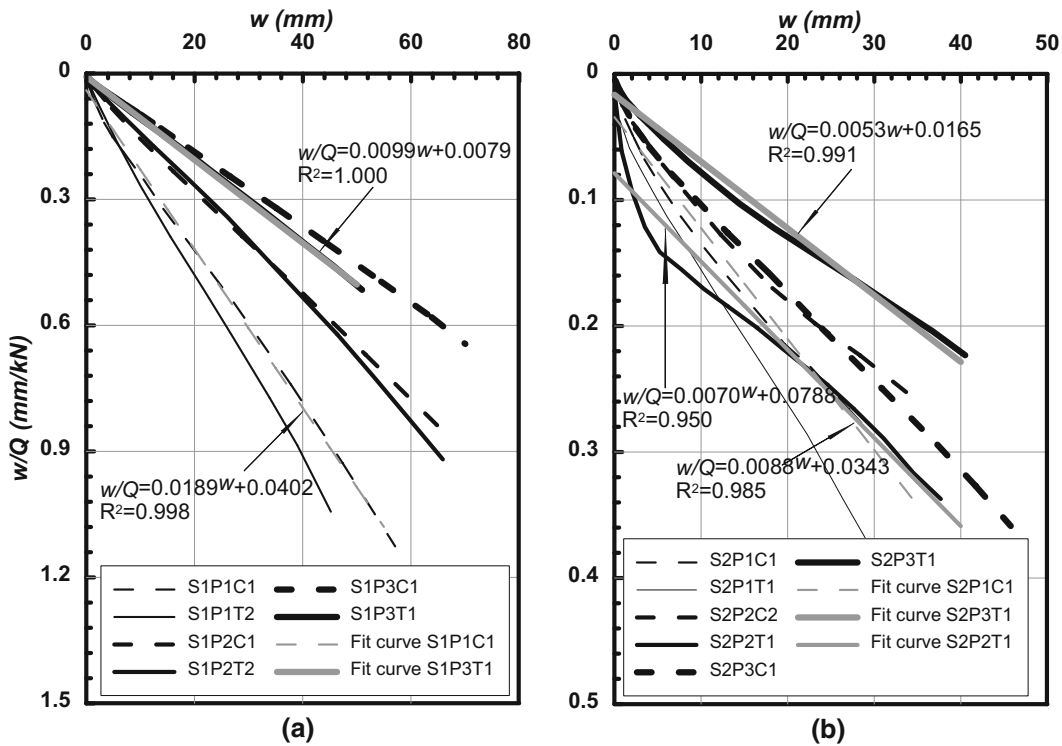


Fig. 9 w/Q versus w curves of test results at the loading stage

coefficients of determination R^2 of the linear regression are also presented in Table 2. It shows that the curves from Site 1 have higher R^2 than those from Site 2, and the R^2

values for both sites are very close to 1.0, except for a few outliers (e.g., S2P2T1) caused by the soil heterogeneity. The high R^2 confirms that Chin’s hyperbolic assumption

offers a good approach to predicting the Q - w curves of helical piles with a reasonable accuracy.

3.2 Torque factors

The torque was recorded manually per 300 mm penetration during installation. The measured curves of torque (T) versus pile penetration depth (Z) are shown in Fig. 10. The helix is located 0.3 m above the pile tip, so the helix penetration depth Z_H (also shown in Fig. 10) is 0.3 m less than Z . It is shown that T is trivial when the helix is above the ground surface. At Site 1, because the subsurface soil was fairly homogeneous, T generally increased with Z_H . At Site 2, torque profiles were complicated by the soil heterogeneity. The CPT results of Site 2 (Fig. 3) show that q_c increases to 1.4 m BGS and starts to decrease, increases at 2.6 m BGS and decreases again at 3.6 m BGS until it remains constant at 4.2 m BGS where the underlying weak cohesive layer exists. T versus Z_H curves at Site 2 have a pattern similar to q_c profiles: Figure 10d, e shows that T starts to decrease at Z_H of about 1.4 m, and Fig. 10f shows that T values of P3 piles decrease at Z_H 2.0 m and increase again at 2.7 m until 3.7 m which conforms to the behavior of q_c of CPT 1 whose borehole is surrounded by P3 piles. The considerable similarity between q_c and T versus Z_H curves implies that: (1) the torque resistance changes with the soil strength, and (2) the torque resistance against the helix is critical to the total torque resistance.

Hoyt and Clemence [17] proposed a relationship:

$$Q_{ult} = K_t T_f \quad (6)$$

where K_t is the torque factor and T_f is the final installation torque. Equation (6) is a common design method used by the helical pile industry. Torque factors of test piles in the present study are estimated and presented in Fig. 11, classified by the pile type and load direction. At Site 1, the compression and tension capacities have similar torque factors. The P1 piles have the largest K_t of 36 m^{-1} , P2 piles have a smaller K_t of 24 m^{-1} , and the largest P3 piles have the smallest K_t of 15 m^{-1} . This trend is consistent with the observed trend in the literature that K_t decreases with the pile shaft diameter. At Site 2, K_t versus d shows a complicated pattern. The P2 piles have the largest K_t of 54 m^{-1} . This is likely caused by the soil heterogeneity at the depth of helix. Figure 12 presents the soil profile and the embedment of test piles in the vertical cut plane along the layout of the CPT boreholes at Site 2. For P1 and P3 piles at Site 2, the helices were embedded very close to the interface of two layers where the soil strength changed dramatically. Therefore, a significant uncertainty is introduced to the T_f of P1 and P3 piles as shown in Fig. 10d and f. The average K_t values of P1 piles for compression are lower than expected because the low-strength underlying layers reduced the bearing capacity of the helix but did not affect the installation torques. The helices of P3 piles were seated on the boundary between a high-strength sand layer and a low-strength silty clay layer (Fig. 12), and as a result T_f of S2P3C1, S2P3C2, and S2P3T1 are relatively small; S2P3T2 has a high T_f because its helix may not be affected

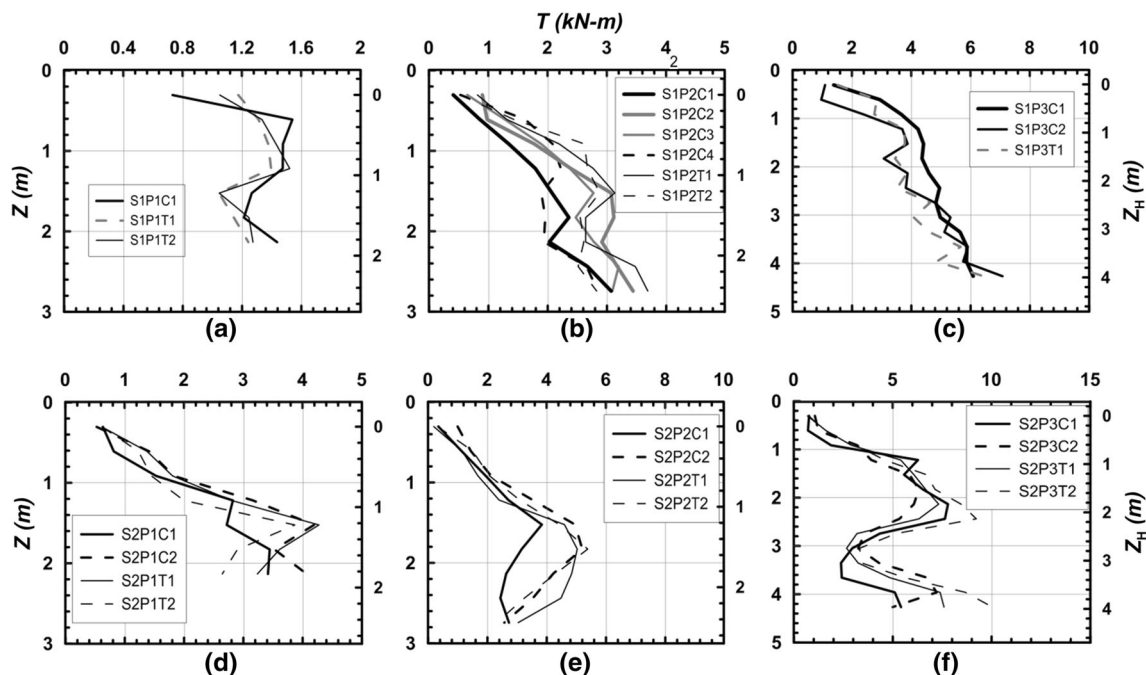


Fig. 10 Installation torque (T) versus tip penetration depth (Z) and helix penetration depth (Z_H)

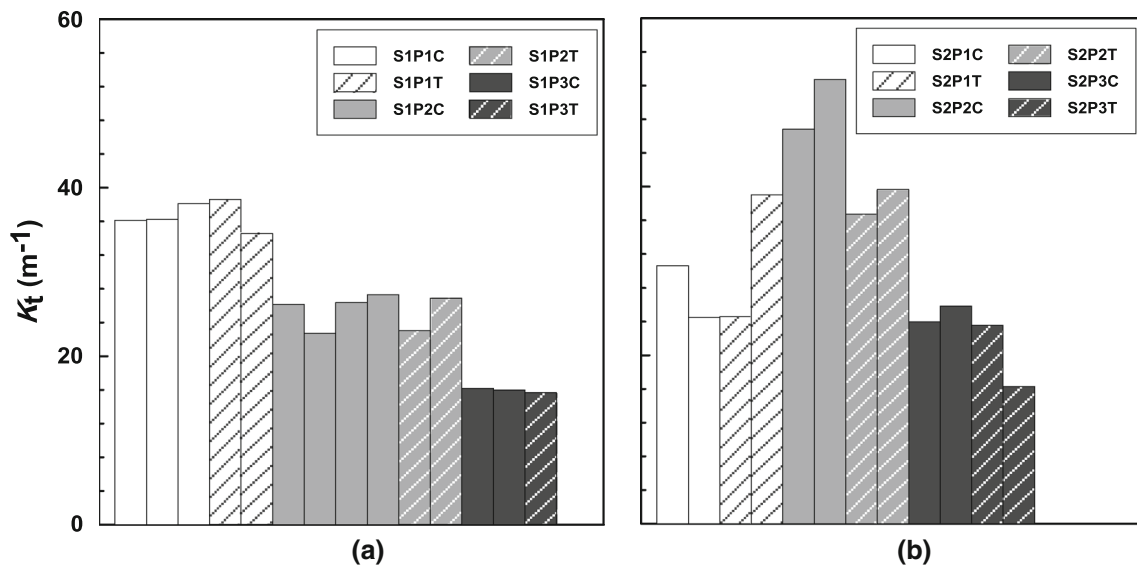


Fig. 11 Torque factors of P1, P2 and P3 at: **a** Site 1 and **b** Site 2

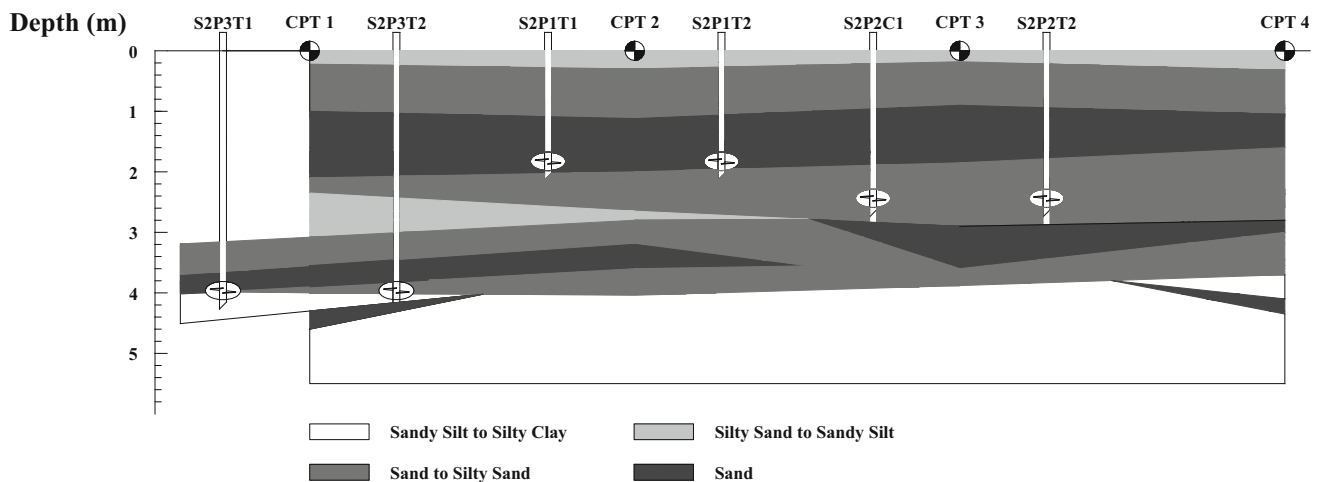


Fig. 12 The soil profile and the helical piles on the vertical cut plane along CPT boreholes

by the low-strength layer. However, there are two high-strength sand pockets overlying and underlying the helices of all the P3 piles which enhanced Q_u to produce a high K_t for S2P3C1, S2P3C2, and S2P3T1. For P2 piles at Site 2, the helices were embedded at the center of a sandy silt to silty sand layer; thus, the measured T_f values of all P2 piles were consistent as shown in Fig. 10e. In addition, the soil strength at the helix embedment depth of P2 piles was at a local minimum so that K_t of P2 piles is high due to low measured T_f (Fig. 10e).

A few axial load tests were conducted on single-helix piles. The K_t values, pile dimension, and soil classification are summarized in Table 3 and shown in Fig. 14. A simple tendency governed by the shaft diameter is delineated: K_t decreases when d increases. However, this tendency

becomes ineffective when the heterogeneous soil strength occurs like Site 2 (Fig. 13).

4 Numerical modeling

A two-dimensional numerical model for the helical pile simulation is developed using the methodology of BNWF on the platform of OpenSees. The BNWF method simplifies the soil–pile interaction to be three sets of nonlinear soil reaction springs. Input parameters for the reaction springs are determined from the soil properties obtained from the subsurface investigation. In the BNWF model, we take the ineffective length l_{ineff} shown in Fig. 14 into consideration. We conducted a parametric analysis by changing l_{ineff} to find out the best estimate.

Table 3 A summary of torque factors of single-helix piles in the literature

References	Soil description	Shaft diam. <i>d</i> (cm)	Helix diam. <i>D</i> (cm)	<i>D/d</i>	<i>E</i> (m)	<i>K_t</i> (m ⁻¹)	Load type
Sakr [26]	Compacted, dense sand	32.4	76.2	2.4	9.5	7.3	C
	Compacted, dense sand	40.6	91.4	2.3	6.1	6.8	C
	Compacted, dense sand	40.6	91.4	2.3	5.7	5	T
	Compacted, dense sand	50.8	101.6	2.0	5.8	7.1	C
Tappenden and Segó [29]	Stiff silty clay	11.4	45.7	4.0	4.0	21.1	C
	Stiff silty clay	17.8	45.7	2.6	4.6	8.3	C
	Firm to stiff clay till overlying clay shale	21.9	40.0	1.8	7.5	8.9	C
	Stiff silty clay	21.9	45.7	2.1	4.6	7.7	C
	Hard clay till	27.3	76.2	2.8	5.9	12.8	C
	Hard clay till	27.3	76.2	2.8	5.9	9.8	T
	Very dense sand till	40.6	76.2	1.9	4.9	7.9	T
Sakr [25]	Dense sand	17.8	40.6	2.3	5.3	23.9	C
	Dense sand	17.8	40.6	2.3	5.1	10.3	T

4.1 Configuration of numerical model

The numerical model consists of an elastic shaft and three sets of nonlinear soil elements: *q-z* (QzSimple1), *t-z* (TzSimple1), and *p-y* (PySimple1) springs. The soil reaction springs are implemented in OpenSees by Boulanger et al. [7, 8]. The *q-z*, *t-z*, and *p-y* springs are characterized by the curves of pile end bearing load versus axial displacement, skin friction versus axial displacement, and lateral resistance versus lateral displacement, respectively. Figure 15 shows the sketch of the BNWF model. The pile shaft below the ground surface and above the top helix is divided into 20-mm-long elements. Each pile node is connected to a fixed node via corresponding soil reaction

springs. The helix is simulated as a horizontal rigid beam crossing the pile shaft; the rigid beam is equally divided into several elements vertically supported by *q-z* springs that simulate the vertical soil-helix interaction. The *p-y* springs are implemented to provide lateral constraints to the pile, but the parameters of the *p-y* springs in this model are non-crucial because the load is axial. The pile shaft is modeled by a linear-elastic uniaxial steel material. The wall thickness of the steel shaft is 7.8 mm, and the Young’s modulus is 200 GPa.

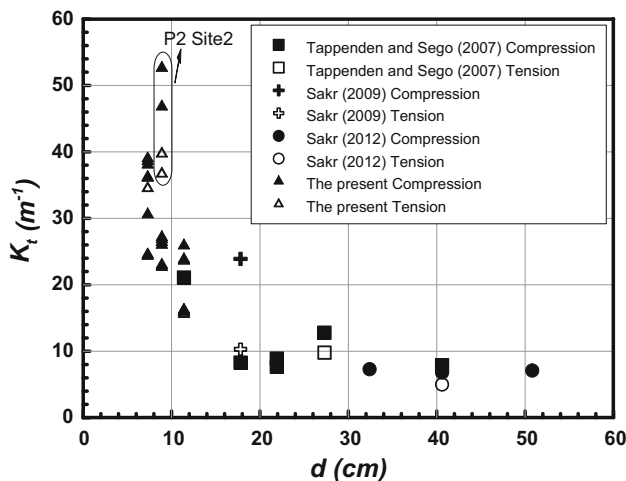


Fig. 13 Summary of torque factors of single-helix piles

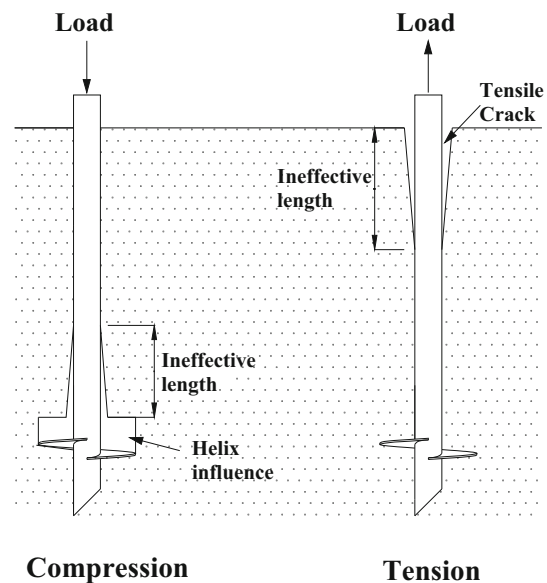


Fig. 14 A sketch of the ineffective zone in axial load transfer of helical piles

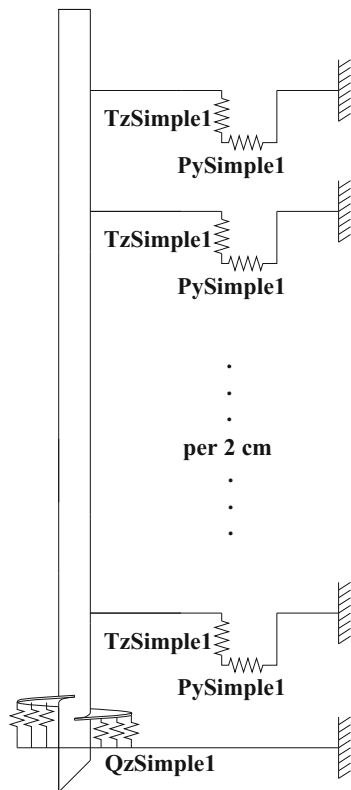


Fig. 15 Numerical model configuration

4.2 Parameterization of soil reaction springs

The input parameters for the reaction springs include the limit capacity (t_L or q_L) and the displacement at half limit capacity (z_{50t} or z_{50q}). For the piles at Site 1, the unit area bearing capacity q_L (kPa) of the helical plate is calculated by:

$$q_L = N_c s_u \quad (7)$$

where N_c is the bearing factor. Aschenbrenner and Olson [6] recommend N_c varying from 0 to 20 and CGS [9] recommend N_c of 9.0 for compression. Meyerhof [19] suggested Eq. (8) for tension:

$$N_c = 1.2 \frac{H}{D} \leq 9.0 \quad (8)$$

where H is the helix embedment depth and D is the helix diameter. Table 4 summarizes the adopted q_L that are slightly adjusted according to the measured bottom and top helix base resistance using strain gauges by Zhang [32] in the same test site. The axial capacity of each q - z spring will be the product of the q_L and the respective helical plate area represented by the spring.

API [3] proposed a value of 10% of the pile end diameter as the critical displacement, z_{cq} , beyond which the bearing or uplift resistance remains constant, and

Table 4 Adopted equations and parameters in the numerical model

		Compression	Tension
Site 1	q_{ult}	$8.0s_u$	$1.0H/D s_u \leq 9.0$ Meyerhof [19]
	z_{50q}	API [3]: $0.09z_{cq}$, where $z_{cq} = 0.1D$	
	t_{ult}	Coyle and Reese [12]	
	z_{50t}		
Site 2	q_{ult}	$N_c \sigma'_v$	$0.74 N_c \sigma'_v$
		N_c from Meyerhof [19]	Das [13]
	z_{50q}	$1.125\%D$ (API [2])	
	t_{ult}	Castello [10]	
	z_{50t}	Mosher [21]	

recommended z_{50q} in clay to be $0.13z_{cq}$. The present model adopted z_{50q} equal to $0.09z_{cq}$ (Table 4), which is slightly smaller than the recommendation of API [3], adjusted by the test results of Zhang [32] and the corresponding interpretation in Li et al. [18]. The adjustment is aimed at calibrating the shape of the computed backbone to approach the measured curve. The adopted t_L and z_{50t} parameters follow the charts recommended by Coyle and Reese [12] proposed for clays based on the undrained shear strength and depth of interests, respectively.

For piles at sandy Site 2, the bearing or uplift capacity of the spring is estimated by:

$$q_L = N_c \sigma'_v \quad (9)$$

The bearing (for compression) and breakout (for tension) factors N_c are estimated using Meyerhof [19] and Das [13], respectively, based on the internal friction angle obtained from the CPT soundings. Vijayvergya [31] recommended the critical displacement, z_{cq} , for pile end bearing ranging from 3 to 9% of helix diameter and API [2] recommended z_{50q} to be 12.5% of z_{cq} .

Castello [10] presented a designed chart to estimate the shear resistance t_L on the pile shaft in sand based on internal friction angle and the ratio of depth to shaft diameter. Mosher [21] proposed a correlation between the friction angle and the initial modulus of t - z curve in sand and determined the half-capacity displacement z_{50t} as the ratio of t_L to the initial modulus. The present model adopted the recommendation of Castello [10] and Mosher [21] when assigning parameters to the t - z curves in sand.

5 Results and discussion

The strength profiles (shown in Figs. 2, 3) and the preceding models for soil reaction springs are incorporated into the BNWF numerical model in OpenSees. It is observed that by neglecting the ineffective zone, it creates

a large gap between the numerical modeling and field test results. Therefore, a parametric analysis is conducted to evaluate the effect of l_{ineff} and determine the best estimate of l_{ineff} . The value of l_{ineff} is varied to be 0, $3D$, $4D$, and $5D$, by eliminating the corresponding amounts of t - z springs within the ineffective zone accordingly.

Figure 16 shows the Q - w curves of the parametric analysis for selected tests S1P3C1 (compression test at Site 1) and S2P3T2 (tension test at Site 2); the measured Q - w curves are also presented for comparison. It is observed that neglecting the ineffective zone (i.e., $l_{\text{ineff}} = 0$) overestimates the axial capacity and the initial stiffness. As l_{ineff} increases, the computed Q_L and k_i decreases. The assumption of $4D$ above the top helix for compression (Fig. 16a) and at the ground surface for tension (Fig. 16b) provides the best agreement with the tests results.

Parametric analyses are also conducted for all other test piles, considering l_{ineff} of 0 and $4D$. Figure 17 shows the modeling results of six test piles against the field test results. Overall, the modeling results agree with the test results despite some discrepancy in the transitional stage, which is less focused than other stages in the present research. A better calibration may require improvement of the soil reaction springs with regard to the difference between conventional piles and helical piles. These test piles cover the entire test configurations. It is shown that, without considering l_{ineff} , the numerical modeling overestimates the axial capacities by 11 to 33%; the initial

stiffness is also overestimated. The discrepancy is higher for the tests in the clay than that in the sand. By inputting l_{ineff} as $4D$, the modeling provides a good agreement with the test results with a reasonable accuracy. Therefore, it is reasonable to claim that the best estimate of l_{ineff} is about $4D$ for both of the compression and tension tests. The present numerical study suggests that the negligence of the ineffective zone may result in higher axial capacity of helical piles and therefore may put the superstructure at risk.

6 Conclusions

The axial load–displacement curves and torque–capacity correlations of 26 single-helix piles installed in cohesive and cohesionless soils in Western Canada are obtained in field load tests. A numerical BNWF model is developed to simulate the axial behavior of the test piles and estimate the ineffective length via parametric analyses. The following conclusions may be drawn.

1. For all of the load tests in the cohesive soils at Site 1, Q_{ult} is equal to Q_L . In the cohesionless soils at Site 2, the limit state has not been reached at axial displacement of 10% of D . The rate of resistance mobilization (in terms of Q/w) is greater for cohesive soils than for cohesionless soils. At Site 2, Q_L of all the test piles are generally greater than Q_{ult} .

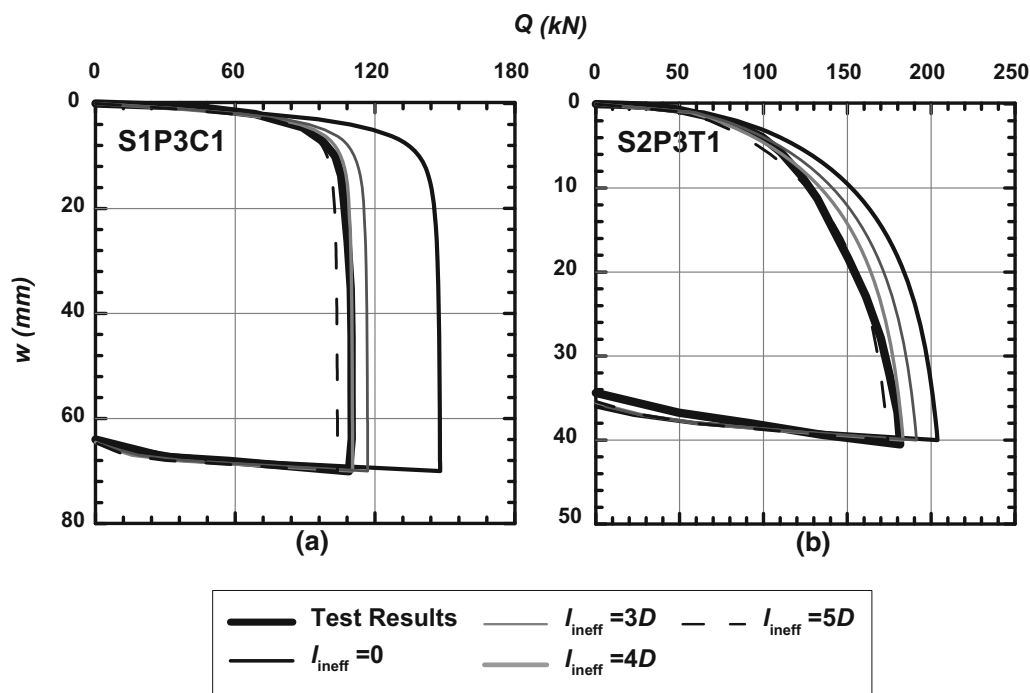


Fig. 16 Effects of the ineffective length l_{ineff} on the Q - w curves

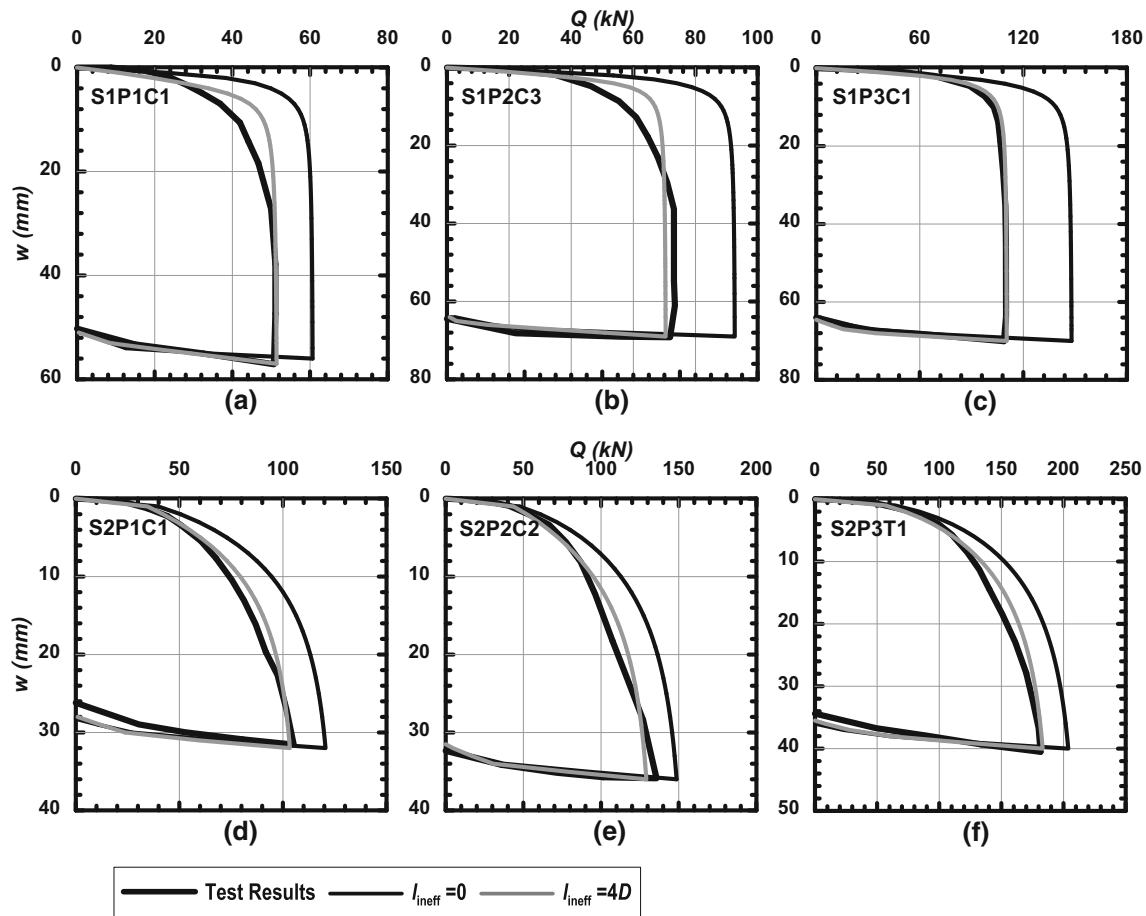


Fig. 17 Comparison of measured and computed axial load versus displacement curves

- In general, Chin's hyperbolic assumption proposed for straight-shaft piles is capable of estimating the axial limit capacities of the helical piles installed in both of the two sites. Chin's hyperbolic assumption offers a good approach to predicting the Q - w curves of helical piles with a reasonable accuracy.
- The torque resistance changes with the soil strength; the helix torque resistance is critical to the total torque resistance. K_t depends on many factors such as shaft diameter, soil types, and load directions. Based on a summary of present and previous test results in the literature, a simple tendency governed by the shaft diameter is delineated: K_t decreases when d increases. However, this tendency may become invalid when there is dramatic change of soil strength near the helix.
- The BNWF method is capable of simulating the single-helix pile subject to axial static loading when a proper ineffective length is assigned. The assumption that l_{ineff} equals $4D$, extending from the top helix upwards for compression or from the ground surface downwards for tension, provides the best agreement between the test and numerical results. The numerical

modeling without considering l_{ineff} overestimates the axial capacity by 11–33%.

Acknowledgements The first author appreciates the financial support of Natural Sciences and Engineering Research Council of Canada–Industrial Postgraduate Scholarship with the contribution of Almita Piling Inc. The authors are thankful to Almita for the permission of publishing the field test results.

References

- Adams JI, Klym TW (1972) A study of anchorages for transmission tower foundations. *Can Geotech J* 9(1):89–104
- American Petroleum Institute (API) (1993) Recommended practice for planning, design, and constructing fixed offshore platforms. API RP 2A-WSD, 20th edn. American Petroleum Institute, Washington
- American Petroleum Institute (API) (2002) API recommended practice 2A-WSD-planning, designing, and constructing fixed offshore platforms-working stress design, 21st edn. American Petroleum Institute, Washington
- American Society for Testing and Materials (ASTM) (2013) ASTM D1143/D1143M. Standard test methods for deep foundations under static axial compressive loads. American Society for Testing and Materials, West Conshohocken

5. American Society for Testing and Materials (ASTM) (2013) ASTM D3689/D3689M. Standard test methods for deep foundations under static axial tensile loads. American Society for Testing and Materials, West Conshohocken
6. Aschenbrenner TB, Olson RE (1984) Prediction of settlement of single piles in clay. *Anal Des Pile Found* 41–58
7. Boulanger RW, Curras CJ, Kutter BL, Wilson DW, Abghari A (1999) Seismic soil-pile-structure interaction experiments and analyses. *J Geotech Geoenviron Eng* 125(9):750–759
8. Boulanger RW, Kutter BL, Brandenberg SJ, Singh P, Chang D (2003) Pile foundations in liquefied and laterally spreading ground during earthquakes: centrifuge experiments & analyses (No. UCD/CGM-03/01). Center for Geotechnical Modeling, Department of Civil and Environmental Engineering, University of California, Davis
9. Canadian Geotechnical Society (2006) Canadian foundation engineering manual, 4th edn. Canadian Geotechnical Society, Richmond
10. Castello RR (1980) Bearing capacity of driven piles in sand. PhD thesis, Department of Civil and Environmental Engineering, Texas A&M University, College Station, TX
11. Chin FK (1970) Estimation of the ultimate load of piles not carried to failure. In: Proceedings of the 2nd Southeast Asian conference on soil engineering, Singapore, 11–15 June 1970, pp 81–90
12. Coyle HM, Reese LC (1966) Load transfer for axially loaded piles in clay. *J Soil Mech Found Div ASCE* 92(SM2):1–26
13. Das BM (2012) Earth anchors. Elsevier, Amsterdam
14. Dilley L, Hulse L (2007) Foundation design of wind turbines in Southwestern Alaska, a case study. In: Proceedings of the Arctic energy summit, Institute of the North, Anchorage, Alaska, 15–18 Oct
15. Godfrey JD (1993) Edmonton beneath our feet: a guide to the geology of the Edmonton region. Edmonton Geological Society, Edmonton
16. Hawkins K, Thorsten R (2009) Load test results: large diameter helical pipe piles. In: Proceedings of the 2009 international foundation congress and equipment expo, 15–19 March 2009. Geotechnical Special Publication No. 185, American Society of Civil Engineers, New York, pp 488–495
17. Hoyt RM, Clemence SP (1989) Uplift capacity of helical anchors in soil. In: Proceedings of the 12th international conference on soil mechanics and foundation engineering, Rio de Janeiro, Brazil. vol 2, pp 1019–1022
18. Li W, Zhang D, Segoo DC, Deng L (2018) Field testing of axial performance of large-diameter helical piles at two soil sites. *ASCE J Geotech Geoenviron Eng* 144(3):06017021-1–06017021-5
19. Meyerhof GG (1976) Bearing capacity and settlement of pile foundations. *J Geotech Eng Div ASCE* 102(3):195–228
20. Malik AA, Kuwano J, Tachibana S, Maejima T (2017) End bearing capacity comparison of screw pile with straight pipe pile under similar ground conditions. *Acta Geotech* 12(2):415–428
21. Mosher, R. L. 1984. Load-transfer criteria for numerical analysis of axially loaded piles in sand. Part 1: Load-transfer criteria, Final Report Army Engineer Waterways Experiment Station, Vicksburg, MS
22. Open System for Earthquake Engineering Simulation (OpenSees) (2016). <http://opensees.berkeley.edu>
23. Rao SN, Prasad YVSN, Veeresh C (1993) Behaviour of embedded model screw anchors in soft clays. *Geotechnique* 43(4):605–614
24. Robertson PK, Cabal KL (2012) Guide to cone penetration testing for geotechnical engineering. Gregg Drilling & Testing Inc., Signal Hill
25. Sakr M (2009) Performance of helical piles in oil sand. *Can Geotech J* 46(9):1046–1061
26. Sakr M (2012) Installation and performance characteristics of high capacity helical piles in cohesive soils. *DFI J—J Deep Found Inst* 6(1):41–57
27. Sakr M (2014) Relationship between installation torque and axial capacities of helical piles in cohesionless soils. *J Perform Constr Facil* 29(6):04014173
28. Salgado R (2008) The engineering of foundations. McGraw-Hill, New York
29. Tappenden KM, DC Segoo (2007) Predicting the axial capacity of screw piles installed in Canadian soils. In: Proceedings of the Canadian geotechnical society (CGS), OttawaGeo 2007 Conference, Ottawa, pp 1608–1615
30. Tsuha CDHC, Aoki N (2010) Relationship between installation torque and uplift capacity of deep helical piles in sand. *Can Geotech J* 47(6):635–647
31. Vijayvergiya VN (1977) Load-movement characteristics of piles. In: Proceedings of Ports'77: 4th annual symposium of the American society of civil engineers, Waterway, Port, Coastal and Ocean Division, Long Beach. ASCE, Reston, VA, vol 2, pp 269–284
32. Zhang D (1999) Predicting capacity of helical screw piles in Alberta soils. MSc thesis, Department of Civil and Environmental Engineering, University of Alberta, Edmonton, AB

Publisher's Note

Springer Nature remains neutral with regard to jurisdictional claims in published maps and institutional affiliations.